

Study of the anisotropy of cosmic expansion on ZTF type Ia supernovae simulations

Barjou-Delayre, C.^{1,*}, Rosnet, P.^{1, **}, Ravoux, C.¹, Aubert, M.^{1,2}, Ginolin, M.³, Kebadian, R.⁴, Amenouche, M.⁵, Bautista, J.⁴, Burgaz, U.⁶, Carreres, B.⁷, Castaneda Jaimes, J.⁸, Dimitriadis, G.⁹, Feinstein, F.⁴, Fouchez, D.⁴, Galbany, L.^{10,11}, Ganot, C.², Graham, M.¹², Groom, S.L.¹³, Goobar, A.¹⁴, Johansson, J.¹⁴, Kasliwal, M.M.⁸, Kim, Y.-L.¹⁵, Müller-Bravo, T.E^{16,17}, Popovic, B.¹⁸, Racine, B.⁴, Regnault, N.¹⁹, Rehemtulla, N.^{20,21,22}, Rigault, M.², Riddle, R.L.²³, Sollerman, J.¹⁴, Townsend, A.²⁴, and Trigui, A.²

(Affiliations can be found after the references)

Received

ABSTRACT

Context. The cosmological principle assumes the isotropy of the Universe at large scales. It is a foundational assumption in the Λ CDM model, which is the current standard model of cosmology. Recent tensions give legitimacy to investigate the possibility of anisotropies in the Universe.

Aims. The large sky coverage achieved by the Zwicky Transient Facility survey (ZTF) allows us to test the veracity of the cosmological principle by using observations of Type Ia supernovae (SNe Ia). In this article, we develop a methodology to measure potential anisotropies in the Hubble constant H_0 . We test our method on realistic simulations of the second data release (DR2) of ZTF-SNe Ia in which we introduced a dipole.

Methods. We develop an unbiased method to introduce a dipole in the simulations as well as to recover it. We test a potential H_0 -dependency of our method and varying the amplitude of the dipole. We analyse the impact of introducing the large-scale structures in the simulations and the efficiency of using a volume limited sample which is an unbiased sample of the ZTF-SN Ia sample. We finally build an error model applied to the recover dipole amplitude (ΔH_0) and its direction (α_0, δ_0).

Results. Our analysis allows us to recover a dipole with an error on the amplitude of $0.33 \text{ km s}^{-1} \text{ Mpc}^{-1}$, and 3.4° & 6.1° for the right ascension and declination, for an initial dipole amplitude of $\Delta H_0 = 3 \text{ km s}^{-1} \text{ Mpc}^{-1}$. The resulting dipole is independent of the chosen H_0 value and sky coverage. This paper paves the way for a future precise ZTF dipole investigation.

Key words. anisotropy – Type Ia supernovae – cosmology

1. Introduction

The Lambda cold dark matter model (Λ CDM) is currently the most accepted to describe the Universe, with numerous agreements with observations. However, some tensions have emerged in the last decade, and certain assumptions can be questioned (Abdalla et al. 2022; Kumar Aluri et al. 2023). The tension on the Hubble constant H_0 is the most striking, reaching a 5σ difference between the early and late universe measurements (Di Valentino et al. (2021)). The late universe measurements are performed using type Ia supernovae (SNe Ia) after calibration of their intrinsic luminosity with the period-luminosity relation of Cepheids. This measurement gives a value of $H_0^{\text{SHOES}} = 73.04 \pm 1.04 \text{ km s}^{-1} \text{ Mpc}^{-1}$ (Riess et al. 2022). The early universe measurements are made using cosmic microwave background (CMB) observations, which are sensitive to the Hubble parameter H at the time of recombination. It is then propagated to our current expansion rate H_0 using Λ CDM. For example, Planck Collaboration et al. (2020) measures: $H_0^{\text{Planck}} = 67.66 \pm 0.42 \text{ km s}^{-1} \text{ Mpc}^{-1}$. The difference between these two measurements could be explained by an alternative cosmological model treating differently the early and late Universe. Alternatively, it can arise from potential systematic errors in the SNe Ia measurement, such as a correlation between the SNe Ia environment and their luminosity (Rigault et al. 2015). Over the years,

other measurements with various methods have been performed (Tip of the Red Giant Branch; Freedman et al. (2025), gravitational lensing of quasar; Chen et al. (2019), Baryon Acoustic Oscillation (BAO) measurements; Abdul Karim et al. (2025)...). The precision of those measurements keeps the debate open, and no known systematic error can explain this tension. More recently, the BAO measurement from the Dark Energy Spectroscopic Instrument (DESI) (Abdul Karim et al. 2025) showed a hint for evolving dark energy, weakening even more the Λ CDM model.

The anomalies of the Λ CDM model (Peebles 2025) give legitimacy to reconsider the main assumptions of this model. Among them, the cosmological principle assumes that the Universe is isotropic and homogeneous at large scales. Conversely, the CMB measurements from COBE (Mather et al. 1990) and Planck (Planck Collaboration et al. 2020) motivate an isotropy violation. This dipole seen in the CMB is generally explained by the motion of the local galactic group (LG) relative to the CMB, due to the gravitational attraction of a nearby over-density (Nusser & Davis 2011). However, the various analyses leaning on this issue computed a significant dipole amplitude, which can not be explained only by the motion of the LG (Bolejko et al. 2016). To explain these measurements, some exotic models have emerged, such as an anisotropic Universe. The Bianchi-I model is the best-known and predicts a quadrupole in the expansion. This model is used in Verma et al. (2024), where the authors found slight evidence for a cosmic preferential axis. More com-

* chloe.barjou-delayre@clermont.in2p3.fr

** philippe.rosnet@clermont.in2p3.fr

plex inhomogeneous models, e.g., the Szekeres Célérier (2024), predict a time and spatial evolution of the Hubble parameter.

Computing the values of H_0 in different directions is a model-independent way of testing anisotropies of the cosmic expansion. With this method Boubel et al. (2025) showed a 3% variation of H_0 using the galaxy catalog Cosmicflows-4 Tully et al. (2023). However, they could not distinguish it from a possible bulk flow. Stiskalek et al. (2025) measured a $4.1 \pm 0.9\%$ H_0 dipole with the Cosmicflows-4 sample and $2.3 \pm 0.6\%$ with the Pantheon+ sample Scolnic et al. (2022a). They show that this dipole came from systematics and not from a real cosmological anisotropy. However, the different analyses do not converge on the same dipole direction or amplitude and the question of potential expansion anisotropy is still under debate.

SNe Ia are well-suited for this type of analysis because their intrinsic luminosity makes them standardizable candles, enabling the determination of H_0 , or the deceleration parameters q , whose anisotropy was studied in Cowell et al. (2023). Studying anisotropies requires a homogeneous survey and a large footprint to conduct analyses in different parts of the Universe while minimizing sky coverage biases. Previous studies have generally been performed on combinations of different SN Ia samples, such as Pantheon+ (Scolnic et al. 2022b), which uses 18 different surveys to form a sample of 1701 SNe Ia in the redshift range $0.01 < z < 2.26$. In our analysis, we mimic the ZTF survey, which gives a homogeneous sampling of SNe Ia in the Northern sky. This survey, and more particularly the second data release (Rigault et al. 2025a), contains 3,628 SNe Ia observed with the same instrument. Using a unique survey is a significant advantage in avoiding calibration issues and ensuring better control of systematic biases. The unique sample of ZTF allows us to compute the value of H_0 in different sky directions. The goal of our analysis is to develop a methodology to fit possible H_0 anisotropies on ZTF realistic simulations, a method that will be applied later on real data.

This article is organized as follows: we present in Sec. 2 the ZTF second SN Ia data release (ZTF SN Ia DR2) and the associated realistic simulation we use in this work. In Sec. 2.3, we detail the SNe Ia standardization process. Sec. 3 gives our method to introduce and fit an H_0 dipole. In Sec. 4, we test for potential systematic effects and parameter variations that could affect our analyses. Finally, in Sec. 5 and Sec. 6 we interpret our results and draw the conclusions of our work.

2. ZTF SNe Ia simulations and standardization

This analysis is based on simulation of the ZTF SN Ia DR2. In this section, we describe the ZTF SN Ia DR2 sample and the simulations of the survey using `skysurvey`. Finally, we explain the standardization of the SNe Ia to use them for a cosmological analysis.

2.1. The second ZTF SN Ia data release

The ZTF survey is a survey of the Northern sky above a declination of -30° (Bellm et al. 2019), using the Samuel Oschin 48-inch Schmidt Telescope based at Palomar Observatory in California (Graham et al. (2019); Dekany et al. (2020); Masci et al. (2019)). ZTF has a large field of view of 47 deg^2 , a camera made of 16 CCD, and uses three filters in the g, r and i-band. ZTF can observe the northern sky in 2 to 3 days. This high cadence provides an excellent light-curve sampling and a typical first detection two weeks before maximum light of an SN Ia, as presented in Rigault et al. (2025b).

In this paper, we simulate the ZTF SN Ia DR2 sample, which compiles SNe Ia detected between March 2018 and December 2020. It is composed of 3628 spectroscopically confirmed SNe Ia, mainly at redshift $z < 0.15$. The Bright Transient Survey (BTS, Fremling et al. (2020); Perley et al. (2020)) complements ZTF with a spectroscopic follow-up. It classifies transient objects and applies quality cuts on the number of observations around peak light and sky visibility, as detailed in Perley et al. (2020). They obtain completeness fractions estimated to 97%, 93%, and 75% for objects brighter than 18 mag, 18.5 mag, and 19 mag, in the three ZTF bands. Most of the ZTF SN Ia DR2 objects are spectroscopically typed with the SED machine (Rigault et al. (2019); Kim et al. (2022); Blagorodnova et al. (2018)). Some spectra are collected from other telescopes, such as LT or P200. The ZTF SN Ia DR2 is described in more detail in Rigault et al. (2025a). As pointed out by the authors in Lacroix et al. (2025), the calibration quality of this sample is insufficient to perform a cosmological analysis. The next data release, named ZTF SN Ia DR2.5, will contain an additional calibration effort. Before applying it on real data, we test our method on realistic simulations of the ZTF SN Ia DR2.5. In a future paper, we will apply this analysis to the ZTF SN Ia DR2.5 sample. In our simulation, we expect that current calibration challenges have been solved and do not try to model the effects described in Lacroix et al. (2025).

2.2. Simulations

To simulate the ZTF SN Ia DR2.5 sample, we use the python package `skysurvey`¹ which generates astronomical targets as a survey would observe them (Amenouche et al. 2025). To mimic observed SN Ia light-curves, we use the SALT2 SN Ia model (Guy et al. 2007, 2010) in its version 2.4 (Betoule et al. 2014). The simulation software also accounts for ZTF observing conditions, detailed in Amenouche et al. (2025). We produce 20 independent simulations of the ZTF SN Ia DR2.5 data set by using the SN Ia rate measurement of ZTF, equal to $2.35 \times 10^{-4} \text{ Gpc}^{-3} \text{ yr}^{-1}$ (Perley et al. 2020). For each simulated SN Ia, its stretch, x_1 , which corresponds to the width of the light-curve, is generated from a bimodal Gaussian distribution following Ginolini et al. (2025b). The SN Ia color c , defined as the difference in magnitude between B and V bands (Phillips 1993; Tripp 1998) follows a Gaussian with a distribution tail (Ginolini et al. 2025a; Scolnic & Kessler 2016).

We generate approximately the same number of SNe Ia as in the ZTF SN Ia DR2.5 sample. This is performed after applying the same cuts as for observations and detailed in Amenouche et al. (2025): $x_1 \in [-3, 3]$, $c \in [-0.2, 0.8]$, $\sigma_{x_1} < 1$, $\sigma_c < 0.1$, $\sigma_{t_0} < 1$, where t_0 is the peak-luminosity date in MJD, and a fit probability greater than 10^{-7} . Once generated by `skysurvey`, the light-curves are fitted with the `sncosmo`² library. To reproduce data quality cuts, we keep only SNe Ia with at least seven detections, including two light-curve pre-peak and two post-peak detections, and we require detection in two different filters within the phase range $\phi \in [-10, 40]$, where ϕ is the time difference in days between a light-curve point and the peak position (t_0). We reject all the detections with a signal-to-noise ratio lower than 5, as for the ZTF SN Ia DR2.5, using the same error on the flux

¹ <https://github.com/MickaelRigault/skysurvey>

² <https://github.com/sncosmo/sncosmo>

presented in Amenouche et al. (2025):

$$\sigma_f = \sqrt{s_b^2 + \frac{|f|}{\text{gain}} + (f \times \sigma_{\text{calib}})^2} \quad (1)$$

where s_b is the sky brightness, f the simulated flux, gain is the CCD gain equal to ≈ 6.2 , and σ_{calib} the calibration precision of ZTF SN Ia DR2.5 equal to 0.025, 0.035 and 0.06 for respectively the g , r and i band. The observing logs are used to reproduce the cadence of observation. These logs contain the field of observation, the limiting magnitude, and any possible technical issues.

At first for the analyses detailed in Sec. 3.2 we used these 20 simulations which do not include the large-scale structure. In a second place, the `skysurvey` software can also generate SNe Ia following an input halo catalog. In that case, the effect of large-scale structure evolution is included, and each SN Ia has an associated peculiar velocity. With this method, we create 27 simulations of ZTF SN Ia DR2.5, which include large-scale structures, using a halo catalog from the Uchuu N-body simulation (Ishiyama et al. 2021). This simulation has a box size of $2 \text{ h}^{-1} \text{Gpc}$ and is cut into 27 sub-grids to reproduce the volume of the ZTF survey, as made in Carreres et al. (2023). This reduction gives a maximal redshift of 0.11 for each SN Ia simulation. To cover the $z > 0.11$ range, the SNe Ia radial peculiar velocities are drawn randomly from a Gaussian distribution with a 250 km s^{-1} dispersion. In our study, we aim to see the impact of the SNe Ia peculiar velocities. We do not correct the peculiar velocities as in Carreres et al. (2025); we leave this analysis for a future paper. Those simulations which include large-scale structures will only be used in Sec. 4.3.

2.3. Cosmological distances from SNe Ia

SNe Ia are not perfect standard candles; thus, they need to be standardized to be used for accurate cosmology. The standardization process is performed using the SALT2 parameters presented in Sec. 2.1: x_1 , c , and x_0 , the overall light-curve amplitude. We use the widely-known Tripp relation:

$$\mu_{\text{obs}} = m_B - M_B + \alpha x_1 - \beta c, \quad (2)$$

where $m_B = -2.5 \log_{10}(x_0) + 10.5$, the constant 10.5 is determined by `sncosmo` for the SALT2.4 model, β is the color coefficient, α the stretch coefficient, and M_B is the absolute SN Ia magnitude in the B -band. This standardization aims to correct the SNe Ia diversity to use them as standard candles. To do so, we fit the standardization parameters as follows: M_B , α , β from the observed distance modulus μ_{obs} . Compared to Ginolini et al. (2025b), we do not use the γp term from SN Ia environmental dependencies because we do not include the SN Ia environment in our simulations. For cosmological analysis, we compute the distance modulus of a SN Ia from the luminosity distance d_l following:

$$\mu_{\text{cosmo}} = 5 \log(d_l \text{Mpc}) + 25; \quad (3)$$

In the context of a flat Λ CDM model:

$$d_l = \frac{c}{H_0} (1+z) \int_0^z \frac{d\zeta}{\sqrt{((1+\zeta)^3 - 1)\Omega_m + 1}}, \quad (4)$$

where c is the speed of light, Ω_m is the matter density parameter. For H_0 and Ω_m we used the `Planck18` values (Planck Collaboration et al. 2020): $H_0 = 67.66 \text{ km s}^{-1} \text{ Mpc}^{-1}$ and $\Omega_m = 0.30966$.

After the SN Ia light-curve fit, we fit the standardization coefficients β , α , M_B by using the following log-likelihood:

$$\mathcal{L}(\alpha, \beta, M_B, \sigma_{\text{int}}) = -\frac{1}{2} \sum_{i=1}^{N_{\text{SNIa}}} \left(\frac{\mu_{i,\text{obs}} - \mu_{\text{cosmo}}(z_i)}{\sigma_i} \right)^2 + \log(2\pi\sigma_i^2), \quad (5)$$

with N_{SNIa} the number of SNe Ia in the simulation survey and σ_i the distance modulus uncertainty given by:

$$\sigma_i = \sqrt{\sigma_{\text{SALT},i}^2 + \left(\frac{5\sigma_{z_i}}{(1+z_i)\log(10)} \right)^2 + \sigma_{\text{int}}^2}, \quad (6)$$

with $\sigma_{\text{SALT},i}$ the error of the SALT2 fit:

$$\sigma_{\text{SALT},i}^2 = \sigma_{m_{B,i}}^2 + \beta^2 \sigma_{c,i}^2 + \alpha^2 \sigma_{x_1,i}^2 - 2\beta V_i(m_B, c) - 2\beta\alpha V_i(c, x_1) + 2\alpha\beta V_i(x_1, m_B), \quad (7)$$

where $\sigma_{m_{B,i}}$, $\sigma_{c,i}$, $\sigma_{x_1,i}$ are the errors of the SALT parameters. V_i is the covariance matrix provided by SALT, here $\sigma_{z_i} = 5 \times 10^{-4}$ is the uncertainty on SN Ia redshift. We do not account for the peculiar velocity uncertainties even when we introduce the large-scale structures in the simulations. Finally, σ_{int} is the intrinsic scatter of the SN Ia magnitude which account for unknown dispersion effects. This parameter is fitted along with α , β and M_B in the likelihood of Eq. 5.

3. Study of a dipole anisotropy of the Hubble constant

3.1. Methodology to introduce a dipole

This section explains how we use a simulated ZTF sample, without the large-scale structure integrated in the simulations, to study a possible anisotropy in H_0 . We test three methods to introduce a dipole in H_0 : at the level of the luminosity distances d_l , the redshift z , and the absolute magnitude m_B .

3.1.1. Dipole introduced in luminosity distance: d_l -method

The most rigorous way to introduce a dipole effect is through the luminosity distance d_l according to:

$$d'_l = \frac{c(1+z)}{H'_0} \int_0^z \frac{d\zeta}{\sqrt{((1+\zeta)^3 - 1)\Omega_m + 1}}, \quad (8)$$

with $H'_0 = H_0 + \Delta H_0 \cos((\Delta\theta))$, where $\cos(\Delta\theta) = \sin(\delta_0) \sin(\delta_i) + \cos(\delta_0) \cos(\delta_i) \cos(\alpha_0 - \alpha_i)$ with α_i , δ_i the equatorial position (RA, DEC) of the SN Ia and α_0 , δ_0 the position of the dipole direction, and ΔH_0 is the amplitude of the dipole. The value of the Hubble constant H_0 is the same as the one in Sec. 2.3. This method does not rely on any specific assumption but is computationally expensive. Indeed, because the SN Ia luminosity distance is set during the simulation stage, a new simulation is required for each dipole direction.

3.1.2. Dipole introduced in the redshift: z -method

To overcome the computational issue of the d_l -method, we propose an alternative method based on the redshift modification after the simulations of SN Ia light-curves:

$$cz = H_0 d \rightarrow cz' = H'_0 d = (H_0 + \Delta H_0 \cos(\Delta\theta)) d, \quad (9)$$

$$z' = \left(1 + \frac{\Delta H_0 \cos(\Delta\theta)}{H_0} \right) z, \quad (10)$$

with d the comoving distance, c the speed of light and z the initial redshift of the SN Ia. With $\cos(\Delta H_0)$ as defined in Sec. 3.1.1. This method is only valid for very low redshifts as it uses the simplified Hubble relation. However, it is still used in literature. Here, we aim to prove that this method gives biased results even for a low-redshift survey.

3.1.3. Dipole introduced in the magnitude: m_B -method

As the previous method, the last one allows to avoid the computational issue of the d_l -method. It consists in changing the simulated SN Ia magnitude in the B -band, m_B , after the simulation of the SNe Ia, using:

$$\mu = 5 \log(d_l) + 25 = m_B - M_B \rightarrow \mu' = 5 \log(d'_l) + 25 = m'_B - M_B, \quad (11)$$

$$d'_l = \frac{c(1+z)}{H'_0} \int_0^z \frac{d\zeta}{\sqrt{((1+\zeta)^3 - 1)\Omega_m + 1}} = \frac{H_0}{H'_0} d_l, \quad (12)$$

$$\mu' = 5 \log(d'_l) + 25 + 5 \log\left(\frac{H_0}{H'_0}\right) = \mu + 5 \log\left(\frac{H_0}{H'_0}\right). \quad (13)$$

By making the difference between μ and μ' , we finally obtain:

$$m'_B = m_B + 5 \log\left(\frac{H_0}{H'_0}\right), \quad (14)$$

with $H'_0 = H_0 + \Delta H_0 \cos(\Delta\theta)$.

We produce a set of 20 simulations of the ZTF footprint, where we apply the z -method and m_B -method, and another set of 20 simulations where we modify the d_l -method at the generation of the SNe Ia also with the ZTF footprint. Our choice of dipole amplitude, for the three methods, is based on taking a midpoint between the early and late universe measurements of H_0 , which is around $70 \text{ km s}^{-1} \text{ Mpc}^{-1}$. The amplitude is defined as the deviation of these central values from both the early and the late measurements, which correspond to $\Delta H_0 = 3 \text{ km s}^{-1} \text{ Mpc}^{-1}$.

3.2. Dipole fitting

We fit the dipole introduced on 20 independent simulations for the three methods introduced in the previous section: the z -method, m_B -method and d_l -method. Our goal is to determine the dipole amplitude (ΔH_0) and its direction (α_0, δ_0), by minimizing the following likelihood :

$$\mathcal{L}(\Theta) = -\frac{1}{2} \sum_{i=1}^{N_{\text{SNIa}}} \left(\frac{\mu_{i,\text{obs}}(\Theta) - \mu_{\text{cosmo}}(\Theta)}{\sigma_i} \right)^2 + \log(2\pi\sigma_i^2), \quad (15)$$

with $\Theta = \alpha, \beta, M_B, \sigma_{\text{int}}, \Delta H_0, \alpha_0, \delta_0$ the free parameters to fit. The fitted amplitude ΔH_0 modifies the luminosity distance of each SN Ia by replacing H_0 in Eq. 4 by:

$$H'_0 = H_0 + \Delta H_0 \cos(\Delta\theta), \quad (16)$$

with H_0 the same value mentioned in Sec. 2.3 and $\cos(\Delta\theta)$ the same as in Sec. 3.1.2.

The analysis is done following these steps, which ensure a good stability for the fitted dipole:

1. We first fit the standardization parameters ($M_B, \alpha, \beta, \sigma_{\text{int}}$) from Eq. 2.

2. We performed a first dipole fit where our only free parameter is the amplitude of the dipole, and we test 12 different positions of the dipole, determined by splitting the sky with a Healpix schema³ ($n_{\text{side}}=1$). This first fit with 12 different dipole positions allows us to determine a preferential area on the sky for a possible dipole. The dipole amplitude and location with the lowest χ^2 value are selected and used as initial parameters for the next fit. This method gives a first estimate of the dipole direction and is necessary for fitting convergence.
3. In a second fit, our free parameters are the dipole parameters (the amplitude ΔH_0 and the coordinate α_0, δ_0) and the standardization parameters M_B, α, β . We used as a fit first guess the values of α_0, δ_0 , and ΔH_0 determined from the previous step. The nuisance parameter M_B is degenerate with H_0 , which implies a correlation with dipole amplitude as detailed in Appendix A. For this reason, we have to fit the standardization parameters at the same time as the dipole parameters.
4. The third fit consists in fitting the σ_{int} only, with the values of M_B, α, β and the dipole fixed from previous fit. We have to fit σ_{int} independently, because fitting it with M_B, α, β introduces a bias in their values as shown in (Kowalski et al. 2008).

This methodology provides a data-based approach that allows probing all directions in the sky without any assumptions. As we focus only on comparing the three methods in this section, we use the x_1, c and x_0 generated from the simulations.

3.3. Dipole fit results

The fit result for an input dipole of amplitude $\Delta H_0 = 3 \text{ km s}^{-1} \text{ Mpc}^{-1}$ and a direction $\alpha_0 = 90.0^\circ$ and $\delta_0 = 19.5^\circ$ is shown in the skymap representation for the m_B -method in Fig. 1. The orange triangle corresponds to the 20 fit for the 20 different simulations, the results are close to the true value in black stars. We show the fitted value for the amplitude and direction with the three dipole introduction methods in Fig. 2. Our fit gives unbiased dipole location (α_0, δ_0) for the three methods, considering the median absolute deviation (MAD) of the 20 independent simulations, represented by a gray band in the plot. For the amplitude ΔH_0 , the z -method is giving a bias of $\approx 6\%$. We interpret this bias to be caused by the low-redshift approximation of the Hubble law, which starts to deviate by 4% in luminosity distance from ΛCDM at $z = 0.06$.

To quantify the impact of the introduced dipole direction, we perform the same procedure for 48 different dipole positions. We evenly distribute those positions by cutting the sky with a Healpix scheme ($n_{\text{side}} = 2$), as shown in Fig. 3. We used the center of the 48 patches as input dipole directions, each tested with the three introduction methods. Similarly, we use for every directions an amplitude of $\Delta H_0 = 3 \text{ km s}^{-1} \text{ Mpc}^{-1}$.

The results for the 48 introduced dipoles are shown in Fig. 4. The green stars represent the z -method, the blue triangle represents the m_B -method, and the pink dot represents the d_l -method. We represent the median of the 20 simulations for each dipole. We can observe a slope in the amplitude for the three methods. Unlike the two other methods, the d_l -method shows a different slope direction. However, the m_B and d_l -methods amplitudes are still contained in the error bar represented by the pink band and calculated from the median absolute deviation (MAD) over the different simulations. We use the MAD instead of the standard deviation to reduce the influence of outliers, and for

³ <https://healpix.sourceforge.io/documentation.php>

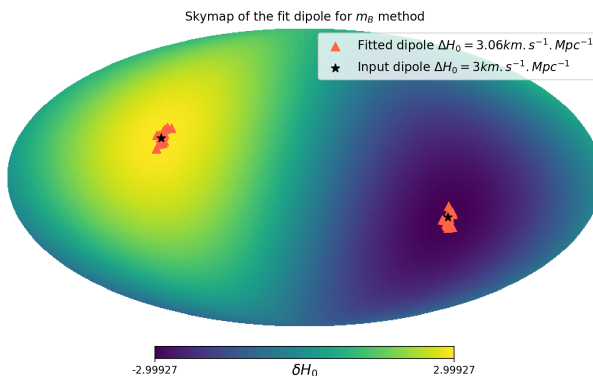


Fig. 1. Skymap colored following the amplitude of the dipole, with the black stars representing the initial dipole direction of an amplitude of $3 \text{ km s}^{-1} \text{ Mpc}^{-1}$. The orange triangles are the fit directions for the 20 simulations when the m_B -method is used. The fitted amplitude in the legend corresponds to the median value over the 20 simulations.

consistency with the median estimator used to compute the difference between the output and input. The z -method produces a large bias in amplitude. Taking the median of the 48 dipole direction for the three methods, the z -method gives an average bias of $0.134 \text{ km s}^{-1} \text{ Mpc}^{-1}$ compared to the m_B -method, which is $0.004 \text{ km s}^{-1} \text{ Mpc}^{-1}$. This result confirms our previous conclusion about the non-robustness of the z -method compared to the other two. For the d_l -method, we must generate as many simulations as the introduced dipole, making it computationally expensive. The m_B -method is a good compromise between an unbiased fit and numerical efficiency. For this reason, we use this method from now on.

Fig. 5 shows the fit results for the 20 simulations and 48 input dipole positions, but using the x_1 and c parameters fitted by SALT instead of the generated ones. Each patch is color-coded by the median of the difference between the output of the fit and the input of the amplitude ($3 \text{ km s}^{-1} \text{ Mpc}^{-1}$ for the 48 introduced dipole). We observe that the dipole amplitude is underestimated at the bottom right and overestimated at the top left by an order of $0.1 \text{ km s}^{-1} \text{ Mpc}^{-1}$, meaning we have more difficulty fitting the dipole near the equatorial poles. These results are visible as a slope in Fig. 4. This slope is visible for the three different methods, and its origin is investigated in more detail in Sec. 4.2 and seems to be caused by the ZTF cadence of observations.

In Fig. 5, the gray ellipses are centered around the median of the 20 fitted location dipole, and the crosses represent the position of the introduced dipole. All the cross are in the 1σ ellipse, which confirms that the fit is still unbiased in terms of dipole position, whatever is the direction. The crosses are colored as a function of the median of their sensitivity ($\Delta H_0 / \sigma_{\Delta H_0}$), which is lower near the pole of the map $\Delta H_0 / \sigma_{\Delta H_0} = 15$. It implies an increased difficulty in retrieving the amplitude on this side of the map, mainly caused by an increase in the amplitude uncertainty.

To estimate an error bar associated with our measurement, we choose to remain conservative by keeping the largest uncertainties associated with the MAD of the 20 simulations. It gives $\sigma_{\Delta H_0} = 0.19 \text{ km s}^{-1} \text{ Mpc}^{-1}$ for the amplitude, $\sigma_{\alpha_0} = 8.8^\circ$ for the right-ascension and $\sigma_{\delta_0} = 3.9^\circ$ for the declination. With a more optimistic error bar estimation, taking the median of the MAD, we obtain respectively $0.11 \text{ km s}^{-1} \text{ Mpc}^{-1}$, 1.9° , and 2.9° . Even with the conservative estimator, we largely recover the amplitude of the initial dipole introduced in the simulations: $\Delta H_0 = 3.01 \pm 0.19 \text{ km s}^{-1} \text{ Mpc}^{-1}$.

4. Systematic studies and parameter variations

In this section, we investigate different systematics which can impact our interpretations and we vary the introduced parameters.

4.1. Varying the Hubble constant

In the previous sections, we measured the dipole values from 48 different orientations, but assuming the Planck18 H_0 value. As mentioned in the Sec. 1, the Hubble constant value is debated. Thus, we perform our analysis considering different H_0 values in the fit, while we keep the H_0 value of the simulation fixed. The objective is to check that our analysis is not sensitive to the choice of the H_0 value assumed in the fit. The results are shown in Fig. 6. We can observe that the behavior is the same between the three values. The error are exactly the same for the three different values. We conclude that our fitting methodology is not impacted by the choice of H_0 value in the fit.

4.2. Sky Coverage

We analyzed different sky coverage scenarii to check for any bias introduced by the SN Ia distribution. Indeed, even if ZTF covers a large part of the sky, its anisotropic sky coverage could introduce bias. We create fives new sets of simulations, keeping the same statistics than in the ZTF SN Ia DR2 ($\approx 3,600$ SNe Ia):

- one with an isotropic distribution of SNe Ia in the sky without cut on the Milky Way (MW). Represented in deep pink dot in the Fig. 7.
- one with a full sky but a cut on the MW represented in blue in Fig. 7
- another with a cut in MW and below -30° in declination to reproduce the ZTF sky coverage but without any SN Ia selection cut, represented in yellow in Fig. 7.
- one with a cut in MW and a cut below -30° in declination to reproduce the ZTF sky coverage, and with the function selection that reproduces the spectroscopic follow-up of BTS, as explained in Sec. 2.1, in purple in Fig. 7
- a last one with the ZTF skymap and the observing logs containing all the observation information, in orange in Fig. 7.

As we focus only on testing the impact of the footprint, we choose to use the stretch x_1 , color c , and x_0 generated parameters in the fit of those new simulations. For each set of sky coverage, we simulate 20 independent simulations, introduce the dipole with the m_B -method, and fit it with the same procedure as in previous sections. Fig. 7 shows the difference between output and input for the amplitude of the dipole; the right ascension and declination are shown in Appendix B.

If we consider the full sky, the MW cut, and the cut below -30° , the amplitude is unbiased, as in Kalbouneh et al. (2025). The coverage of the sky does not seem to introduce a bias. However, the error for the anisotropic case is slightly bigger: $\sigma_{\Delta H_0} = 0.073 \text{ km s}^{-1} \text{ Mpc}^{-1}$, $\sigma_{\Delta H_0} = 0.090 \text{ km s}^{-1} \text{ Mpc}^{-1}$, respectively for the whole sky and anisotropic sky.

The slope in Sec. 3.2 in the amplitude appears only when we add the effect of the observing log, which contains possible technical issues and the cadence of observations. We interpret that the difficulty in recovering the signal for the amplitude at the pole comes from the cadence of the observation and not from the lack of observations below -30° . We also observe oscillations for all different sky coverage scenarios as a function of the initial location of the dipole. These residual oscillations seem

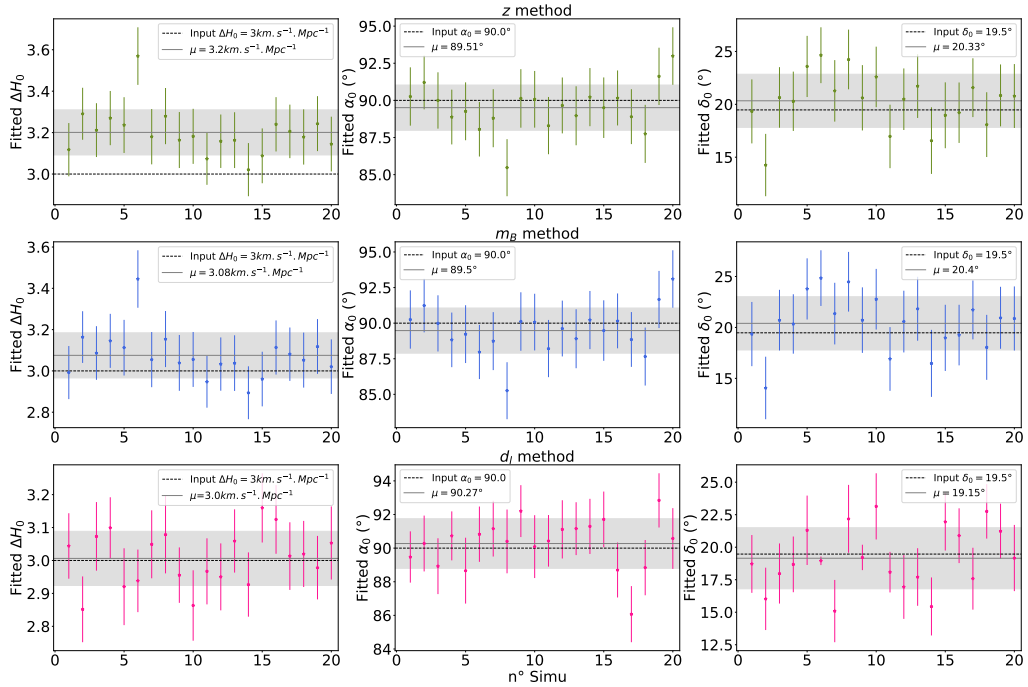


Fig. 2. Fit for the z -method on the top panel, the m_B -method on the middle, and the d_l -method on the bottom. Left to right, the result for the 20 simulations for the dipole amplitude, ΔH_0 , the right ascension, α_0 , and the declination, δ_0 . In each panel, the initial value is represented with the black dashed line, and the median of the twenty simulation fits is in the gray line with the 1σ error represented by the gray band. For those fits, the SNe Ia colors and stretches are the ones input in the simulations.

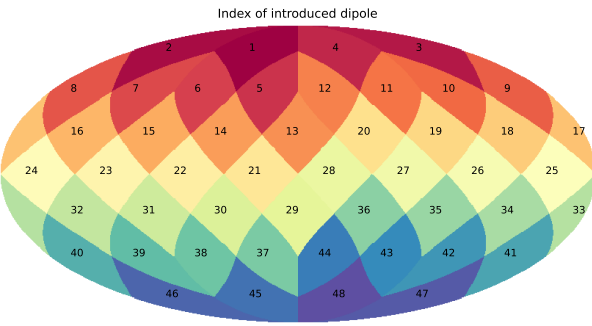


Fig. 3. Skymap with the number of the initial dipole introduced. We used the center of each different patches here to obtained the 48 different dipole location. The color of each patches allow to differentiated the 48 different location of dipole.

to be caused by unexplained small correlations between M_B and α_0 parameters for the whole sky, and amplified by a correlation between α_0 and δ_0 for the realistic ZTF simulations. These oscillations will be investigated further in a future analysis with the data. However, we bring more elements in their potential origin in Appendix B. In spite of their presence, since they remain well below the median error of the simulations, we consider this residual oscillation as negligible.

4.3. Large-scale structure impact

The peculiar velocities shift the observed redshift of SNe Ia (Careres et al. 2023). Including the effect of peculiar velocities, generated from a realistic N-body simulation, allows us to reproduce the ZTF SN Ia DR2.5 dataset more realistically. With the large-scale structure implemented, we run 27 independent simulations. We reproduce the same method as mentioned in Sec. 3.2 for the

m_B -method and for the 48 different introduced dipoles, the results are shown in Fig. 8. We applied a cut on redshift $z > 0.02$, nearby SNe Ia for which the impact of PV is too important and could introduce a bias in the results, as we would do for the real dataset.

For the three dipole parameters, the amplitude and location, we recover the initial value for the 48 different dipoles. As seen in Fig. 8, the difference between the fitted value and the introduced one is included in the 1σ uncertainties. Even if we see a slight offset of $\approx 4.1^\circ$ for the declination, the curve remains included in the uncertainty band. This demonstrates the robustness of the method in recovering the parameters.

For an initial amplitude of $3 \text{ km s}^{-1} \text{ Mpc}^{-1}$, we estimate an amplitude of $3.05 \pm 0.33 \text{ km s}^{-1} \text{ Mpc}^{-1}$. We still have a trend for the difference in the amplitude, but in the opposite direction as compared to the simulations without large-scale structure in Sec. 3.2. The Fig. 8 displays the median values of the 27 different simulations, but considering the simulations one by one, the direction of this slope can be different. Although the orientation of the slope varies from one simulation to another, the slope consistently appears. This indicates that it is unlikely to be a statistical effect and more likely driven by the impact of the ZTF cadence.

4.4. Volume limited

We also tested our method on a volume limited sample, composed of ≈ 1000 SNe Ia with a redshift cut $z < 0.06$ following (Amenouche et al. 2025). It is an unbiased sample where the intrinsic distribution of SN Ia is complete, which means we are less sensitive to the Malmquist bias. Fig. 9 shows the results of the same fit on the large-scale structure simulations, but with the volume-limited sample. Similarly, we also apply the redshift cut $z > 0.02$.

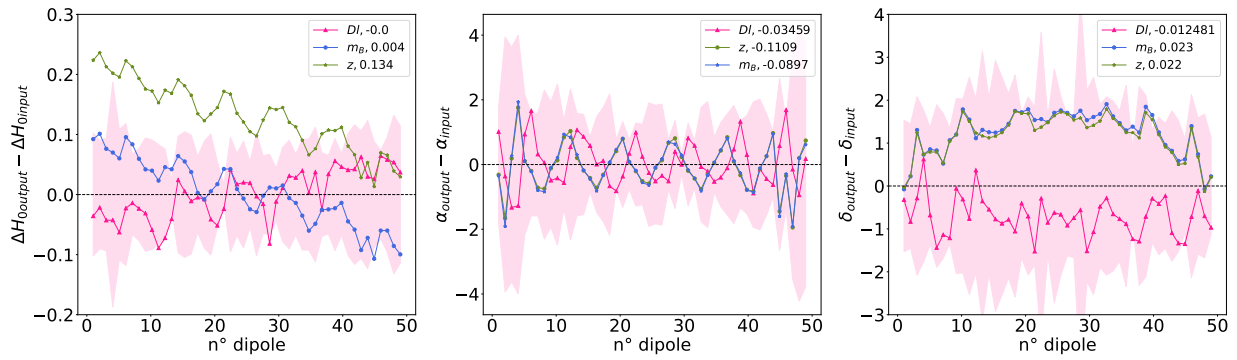


Fig. 4. Difference between the output of the fit and the true value. From left to right for the dipole amplitude, the α_0 , and the δ_0 directions of the dipole. The green line is for the z -method introduced in Sec. 3.1.2, in blue for the m_B -method introduced in Sec. 3.1.3, and in pink for the d_I -method. The pink band corresponds to the typical error for the three methods. The medians are done in the label for the three different methods. As for Fig. 2, the SNe Ia colors and stretches are the ones input in the simulations.

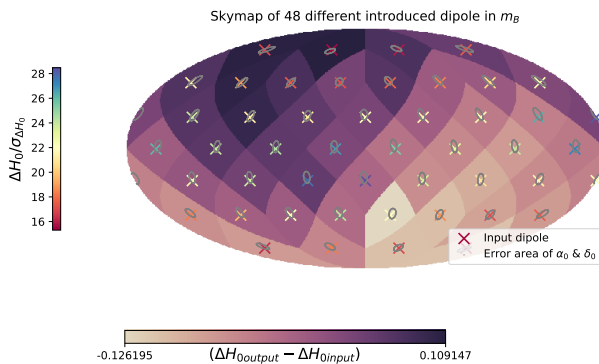


Fig. 5. Skymap of the 48 different dipole fits, with the m_B -method, for 20 independent simulations, and using the SALT color and stretch parameters. Each cross corresponds to the input location of the 48 dipoles, and is colored according to the median of the 20 simulations sensitivity, as shown with the colorbar on the left. Each cross is associated with a patch which is colored according to the median to the difference between the input (here $3 \text{ km s}^{-1} \text{ Mpc}^{-1}$) and output amplitude of the dipole. All the gray ellipses are centered on the median of the different simulation fits, the ellipses represent the 1σ deviations of the fitted direction ($\sigma_{\alpha_0}, \sigma_{\delta_0}$).

The errors are bigger due to a smaller statistic, as we can see in Tab. 1. In addition, we have a bigger offset for the difference between the input declination and output, of 6.5° , but still consistent with the 1σ uncertainties. We conclude that using the volume-limited sample allows us to recover the introduced dipole, but with an increase in the declination offset and in the statistical uncertainty.

4.5. Varying the amplitude

We aim to investigate the dependencies of our study with respect to the input dipole amplitude. We perform the same analysis as before with the following values: $\Delta H_0 = 2 \text{ km s}^{-1} \text{ Mpc}^{-1}$ and $\Delta H_0 = 1 \text{ km s}^{-1} \text{ Mpc}^{-1}$, for the 27 simulations containing the large-scale structure.

Fig. 10 shows the difference between the input and output of the three parameters, and the error of those parameters computed from the MAD. As expected, it is harder to recover the location of the initial dipole introduced for an amplitude of $1 \text{ km s}^{-1} \text{ Mpc}^{-1}$. Indeed, the offset in δ_0 is more pronounced for the smaller amplitude, and the amplitude of the oscillations in

RA is larger. Moreover, the error for this case is more significant than for the other two amplitudes for the dipole position. Focusing on the dipole amplitude in Fig. 10, the error and the difference between the input and output are the same for the three different values. This result confirms the robustness of our analysis and that we can recover a dipole even with an amplitude of $1 \text{ km s}^{-1} \text{ Mpc}^{-1}$, which approximately corresponds to the H_0 error in the direct measurement (Riess et al. 2022).

4.6. Anisotropies study without dipole incorporation in the simulations

We test our methodology in the case when no dipole is introduced in the 27 large-scale structure simulations. We obtain 27 different dipole locations and amplitudes reported in Fig. 11. The highest amplitudes of dipole obtained is $1.2 \text{ km s}^{-1} \text{ Mpc}^{-1}$. However, the MAD for this case is only $0.12 \text{ km s}^{-1} \text{ Mpc}^{-1}$, lower than the one obtained for the three different dipole amplitudes introduced in the simulations in Sec. 4.5 ($\approx 0.34 \text{ km s}^{-1} \text{ Mpc}^{-1}$). The difference between those values results from a systematic error in the initial position of the introduced dipole. Indeed, the slope present for the three different introduced amplitudes in Fig. 10 induces a systematic bias as a function of the initial position of the introduced dipole. We have to take it into account in the total error budget.

We build an error model which is the statistical error, the median of the error of the 27 fits without any dipole in the simulations: $\sigma_{\text{stat}} = 0.16 \text{ km s}^{-1} \text{ Mpc}^{-1}$, and the systematic error from the amplitude slope. To quantify the systematic error, we fit a linear function of the maximum of the slope for the three introduced amplitudes ($1 \text{ km s}^{-1} \text{ Mpc}^{-1}, 2 \text{ km s}^{-1} \text{ Mpc}^{-1}, 3 \text{ km s}^{-1} \text{ Mpc}^{-1}$): $\sigma_{\text{sys}} = f(\Delta H_0)$. We estimate the total error from the quadratic sum: $\sigma_{\text{tot}} = \sqrt{\sigma_{\text{stat}}^2 + \sigma_{\text{sys}}^2}$. We use the same schema to build an error model for α_0 and δ_0 .

We use this error model to compute the error of the previous different analyses in Sec. 4. These errors are summarized in Tab. 1 with their sensitivity. Concerning the result without introducing a dipole in the simulation, for the systematic error we use our linear function extrapolated to a zero amplitude: $\sigma_{\text{sys}} = 0.44 \text{ km s}^{-1} \text{ Mpc}^{-1}$. At the end we have a total error of: $\sigma_{\text{tot}} = 0.47 \text{ km s}^{-1} \text{ Mpc}^{-1}$ for the amplitude, 24° for α_0 and 34° for δ_0 . This means that the large-scale structure imprint a residual pattern that mimics a dipole, but not significant in the error budget.

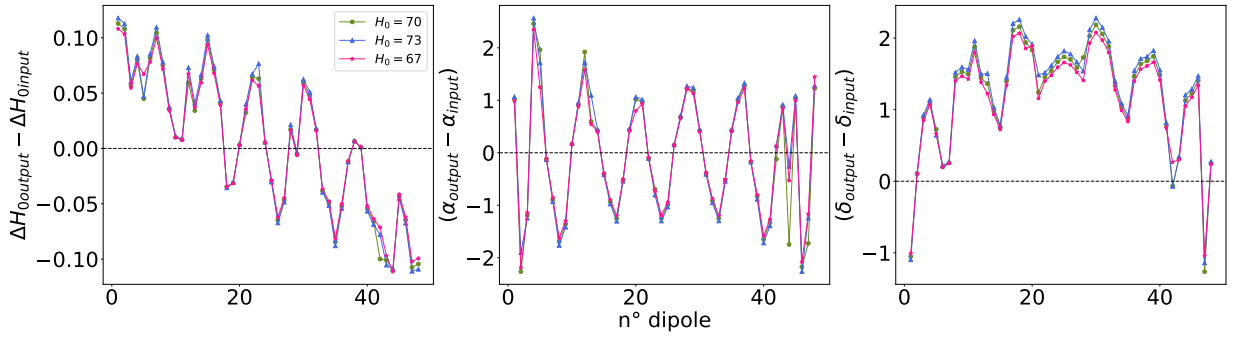


Fig. 6. Comparison of the dipole fit with three different values of H_0 in input: $H_0 = 67 \text{ km s}^{-1} \text{ Mpc}^{-1}$ in pink stars, $H_0 = 70 \text{ km s}^{-1} \text{ Mpc}^{-1}$ in green dots, and $H_0 = 73 \text{ km s}^{-1} \text{ Mpc}^{-1}$ in blue triangles. The top panels show the comparison between the output of the fit and the input as a function of the introduced dipole; each number corresponds to the numbered position in Fig. 3. The bottom panels show the MAD of each parameter as a function of the initial dipole introduced. From right to left, the three parameters represented are the dipole amplitude, the α_0 , and δ_0 directions.

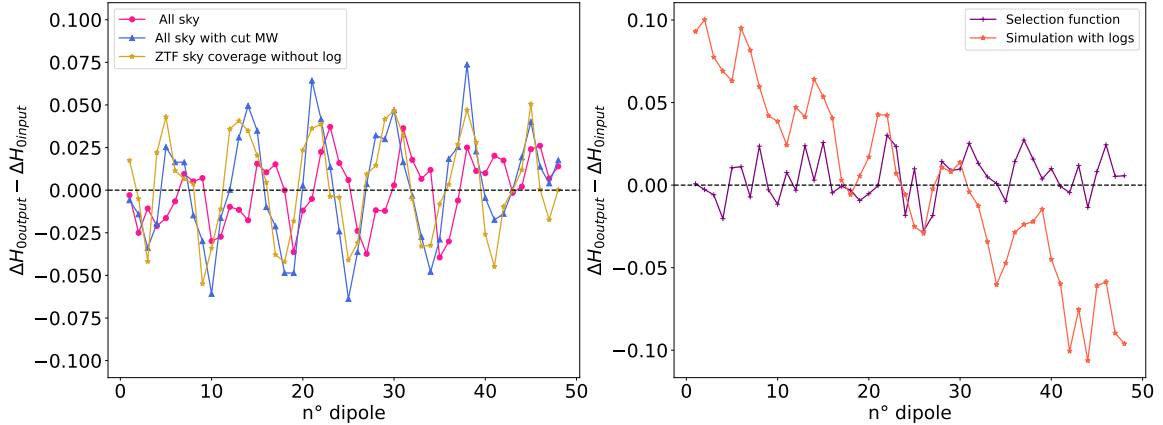


Fig. 7. Difference between the output of the dipole amplitude and its input value ($3 \text{ km s}^{-1} \text{ Mpc}^{-1}$) as a function of the number of the dipole introduced. The different lines show the simulations with increased complexity: (left) All-sky coverage in pink, cutting Milky Way in blue, cutting in addition the south sky in yellow, (right) adding selection function effects in purple, and adding the observation logs in orange.

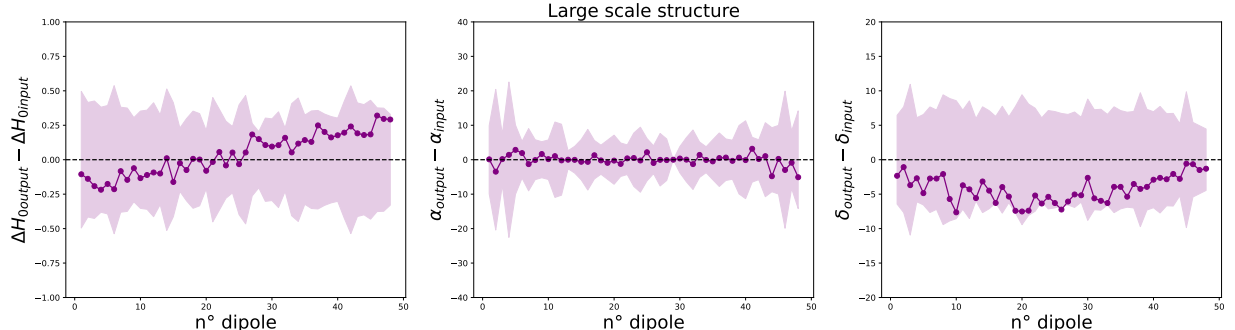


Fig. 8. Difference between the output of the fit and the truth value, for 27 different simulations with the large-scale structures introduced. Left to right, the figure shows the dipole amplitude, the RA, and the DEC. The purple band is the MAD of the 27 simulations centered on zero.

5. Discussion

This analysis aims to build a method to measure a possible H_0 anisotropy and verify the accuracy of the cosmological principle. Our method focuses on a dipole-type anisotropy on H_0 in the ZTF SN Ia DR2.5 sample. We test for various potential systematics and analysis variation, focusing more particularly on the impact of peculiar velocities on our measurement. Indeed, the peculiar velocities caused by the gravitational pull of nearby structures can mimic a bulk flow, i.e., a non-null average velocity in the vicinity of the observer compared to the reference frame. Even with this kind of effect, we can recover a dipole with an am-

plitude of $3 \text{ km s}^{-1} \text{ Mpc}^{-1}$ on ZTF simulation with an accuracy of $0.33 \text{ km s}^{-1} \text{ Mpc}^{-1}$ for an initial amplitude of $3 \text{ km s}^{-1} \text{ Mpc}^{-1}$, and of 3.4° and 6.1° for the right ascension and declination as shown in Tab. 1.

In Sec. 4.6, we perform our analysis without introducing a dipole in the simulations containing large-scale structure effects. This test shows a non-zero amplitude dipole but consistent with zero at one sigma. Even if an H_0 anisotropy is an intrinsic property of the Universe, a H_0 dipole can also be interpreted as a bulk-flow effect in a defined volume. However, in these simulations, a global motion of the observer that would cause a bulk flow is not introduced. This means the residual dipole is

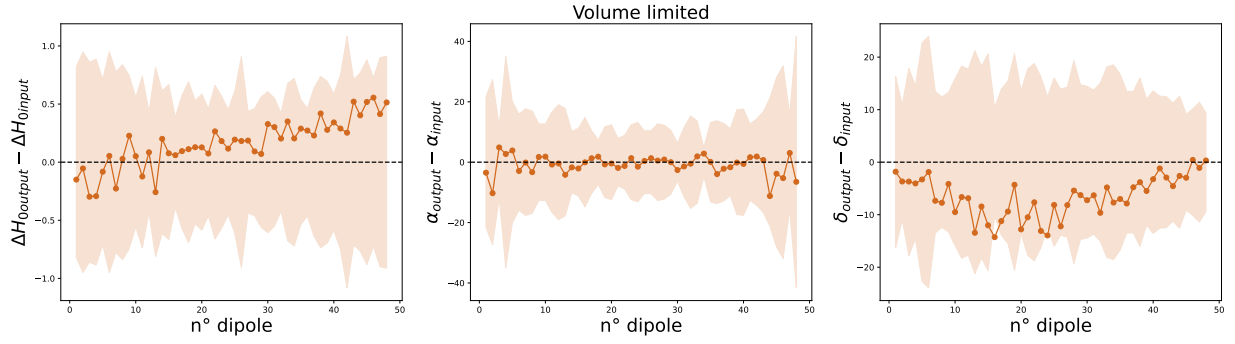


Fig. 9. Same as Fig. 8 for the volume limited sample.

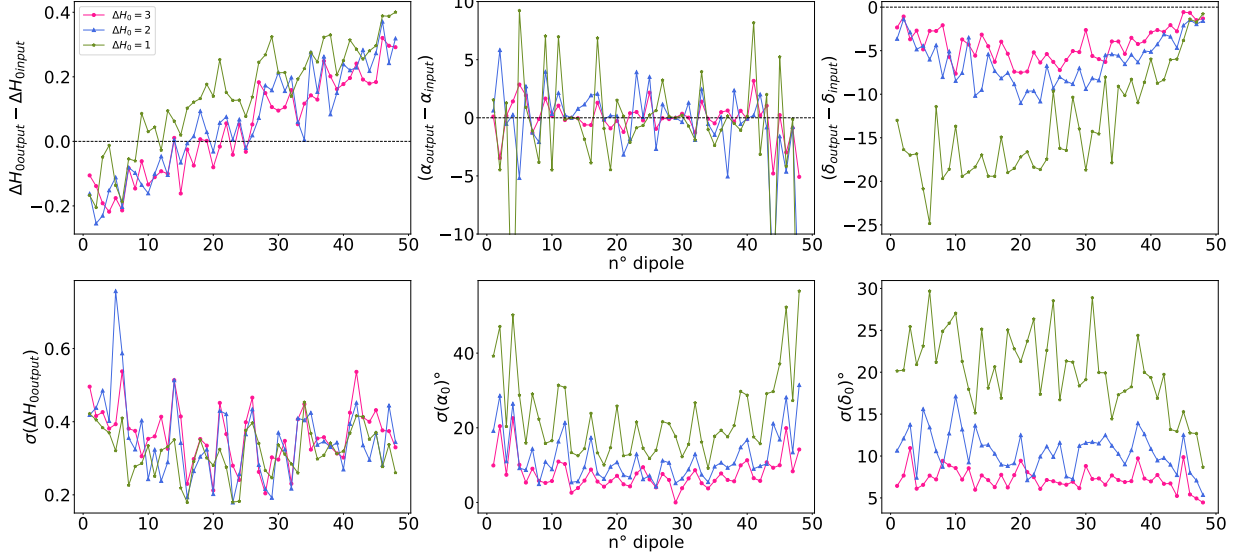


Fig. 10. Comparison of three different values of amplitude of the dipole ΔH_0 in input: $\Delta H_0 = 3 \text{ km s}^{-1} \text{ Mpc}^{-1}$ in pink dot, $\Delta H_0 = 2 \text{ km s}^{-1} \text{ Mpc}^{-1}$ in blue triangles and $\Delta H_0 = 1 \text{ km s}^{-1} \text{ Mpc}^{-1}$ in green stars. The representation of the results is the same as in Fig. 6

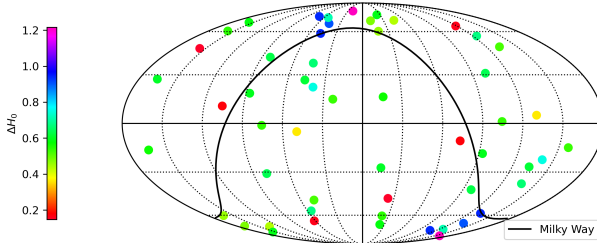


Fig. 11. Skymap of the 27 different fit on simulations without any dipole introduced. Each dots is colored depending the values of the dipole amplitude.

the consequence of peculiar velocities. For future investigation with data, to be able to distinguish a bulk-flow effect from an H_0 dipole, an analysis at different redshifts that covers a large part of the sky will be required.

Some other studies found an H_0 dipole. For example, Migkas et al. (2021) detects an H_0 variation of 9% using galaxy clustering. This variation is equivalent to a dipole amplitude of $6 \text{ km s}^{-1} \text{ Mpc}^{-1}$. As we have a sensitivity of 9 for an amplitude of $3 \text{ km s}^{-1} \text{ Mpc}^{-1}$ in our configuration, we could easily measure these H_0 variations. Other studies detected a quadrupole-type anisotropy, e.g., Cowell et al. (2023). In our article, we limit

Simulation	$\sigma_{\Delta H_0}$	$\frac{\Delta H_0}{\sigma_{H_0}}$	σ_{α_0}	σ_{δ_0}
ΔH_{00}	± 0.47	1	± 24	± 34
ΔH_{01}	± 0.41	3	± 10	± 23
ΔH_{02}	± 0.37	6	± 6.4	± 14
ΔH_{03}	± 0.33	9	± 3.4	± 6.1
$\Delta H_{03}(V_{\text{lim}})$	± 0.42	3	± 17	± 15

Table 1. Sensitivity and error for the different cases analyzed, for the three free parameters of the dipole: the amplitude ΔH_0 in $\text{km s}^{-1} \text{ Mpc}^{-1}$, the location with α_0 and δ_0 in degrees. Here, the sensitivity is the value over the error of the value, with the error built with the error model described in Sec. 4.6. $\Delta H_{01}, \Delta H_{02}, \Delta H_{03}$ correspond to an initial amplitude introduced equal to $1 \text{ km s}^{-1} \text{ Mpc}^{-1}$, $2 \text{ km s}^{-1} \text{ Mpc}^{-1}$, $3 \text{ km s}^{-1} \text{ Mpc}^{-1}$ mentioned in Sec. 4.5 with the simulations containing the large-scale structure. The ΔH_{00} corresponds to the analyses without initial dipole introduced in the simulation discussed in Sec. 4.6. V_{lim} corresponds to the analysis with the volume limited sample detailed in Sec. 4.4 for an initial amplitude of $3 \text{ km s}^{-1} \text{ Mpc}^{-1}$.

ourselves to the study of an H_0 dipole, but future studies should be extended to account for higher multipole orders.

As explained in Sec. 3.2, we estimate the standardization parameters at the same time as the dipole parameters. A con-

firmation of the robustness of the analyses is our ability to recover the standardization parameters used to produce the simulations. The input of the simulations, for a full survey, was: $M_B = -19.3$, $\alpha = 0.14$, $\beta = 3.15$, $\sigma_{\text{int}} = 0.14$. In average for the 48 different dipole locations and 20 simulations, we obtain: $M_B = -19.313 \pm 0.004$, $\alpha = 0.139 \pm 0.003$, $\beta = 3.11 \pm 0.02$, $\sigma_{\text{int}} = 0.128 \pm 0.001$. Regarding the errors, we do not recover the initial parameters. For M_B , which is degenerated with H_0 , its value changes as a function of the H_0 value used in the fit. Concerning α , β and σ_{int} , in this analysis we do not use the complete covariance matrix, we only have the diagonal term, so their uncertainties are underestimated.

All the figures containing the difference between the output parameter and input (see e.g., Fig. 8) show oscillations as a function of the sky position of the introduced dipole. We investigated potential fit issues, which could be caused by boundary effects when the fitted RA value reaches the limit. Changing the reference frame for the fit by centering it on the α_0 value found during the first fit does not affect our results. Furthermore, modifying the fitter limit for RA for the second fit, i.e., from $[0; 2\pi]$ to $[\alpha_1 - \pi; \alpha_1 + \pi]$ where α_1 is the RA guessed during the first fit, has also no impact. These oscillations are included within the error, so are not likely to affect our analysis. Future work will investigate further this effect.

6. Conclusion

This paper details a methodology to measure anisotropy in H_0 in realistic ZTF SN Ia DR2.5 simulations. Our analysis is focused on a dipole anisotropy. We test three methods to introduce the dipole in our simulations; one consisted of introducing it in the redshift of the SN Ia (z -method), the second one introduced the dipole in the compute magnitude of the SN Ia (m_B -method). And the last one introduces it in the luminosity distance (d_l -method). The z -method introduces a bias of $\approx 8\%$ in the recovery of the dipole amplitude. We are not biased for the two others method, but the d_l -method is more expensive numerically. For this reason, we used the m_B -method for all the analyses to implement the dipole in the simulations.

Our conclusions concerning the analysis are the following:

1. Our measurement is affected by the observing logs, which cause a bias in declination in particular. However, the sky coverage, considering the full sky or the ZTF footprint, has no impact on our study.
2. The fitted dipole is not dependent on the H_0 value, both for amplitude and direction.
3. We build an error model containing both statistical and systematic errors, depending on the initial position of the introduced dipole.
4. We are able to recover an anisotropy of an amplitude of $3 \text{ km s}^{-1} \text{ Mpc}^{-1}$, with a precision of $0.33 \text{ km s}^{-1} \text{ Mpc}^{-1}$ for realistic simulations containing large-scale structure. Regardless of the position of the introduced dipole, we recovered it with errors of 3.4° , 6.1° for the right ascensions and declination for a conservative case. The fitted declination is biased $\text{pf} \approx 4^\circ$, but this bias is still contained in the 1σ uncertainties.
5. For smaller dipole amplitudes such as $1 \text{ km s}^{-1} \text{ Mpc}^{-1}$, our errors are larger, and the sensitivity, $\Delta H_0 / \sigma_{\Delta H_0}$, decreases. However, we still recover the signal with a significance of 3σ .
6. Using the unbiased volume-limited sample reduces the sensitivity but gives similar results.

7. We perform our analysis without introducing a dipole in the simulations and then fit a dipole. The fitted dipole amplitude is not consistent with zero, which leads us to believe that we fit a residual dipole from peculiar velocities, but without significance in the error budget.

This first methodology focused on a dipole analysis; another study with a higher multipole, such as a quadrupole, will be investigated in the future. Moreover, this study employs a methodology built on simulations; the application of this method to the ZTF SN Ia DR2.5 data will be the subject of a second study.

The next data release of ZTF, named DR3, will drastically increase the number of SNe Ia to around 10,000. A planned data release with photometrically-typed SNe Ia, named DR4, will increase this number even more to 40,000. Applying our methodology to those data releases will extensively improve the sensitivity and the errors of the analysis. It is also possible to use our method on other present and future surveys such as LSST (The LSST Dark Energy Science Collaboration et al. 2018) or ATLAS (Tonry et al. 2018).

Acknowledgements. Based on observations obtained with the Samuel Oschin Telescope 48-inch and the 60-inch Telescope at the Palomar Observatory as part of the Zwicky Transient Facility project. ZTF is supported by the National Science Foundation under Grants No. AST-1440341 and AST-2034437 and a collaboration including current partners Caltech, IPAC, the Weizmann Institute of Science, the Oskar Klein Center at Stockholm University, the University of Maryland, Deutsches Elektronen-Synchrotron and Humboldt University, the TANGO Consortium of Taiwan, the University of Wisconsin at Milwaukee, Trinity College Dublin, Lawrence Livermore National Laboratories, IN2P3, University of Warwick, Ruhr University Bochum, Northwestern University and former partners the University of Washington, Los Alamos National Laboratories, and Lawrence Berkeley National Laboratories. Operations are conducted by COO, IPAC, and UW. Y.-L.K. was supported by the Lee Wonchul Fellowship, funded through the BK21 Fostering Outstanding Universities for Research (FOUR) Program (grant No. 4120200513819) and the National Research Foundation of Korea to the Center for Galaxy Evolution Research (RS-2022-NR070872, RS-2022-NR070525). U.B and T.E.M.B is funded by Horizon Europe ERC grant no. 101125877. G.D. acknowledges support from the European Union's Horizon Europe research and innovation programme under the Marie Skłodowska-Curie grant agreement No 101199369. L.G. acknowledges financial support from AGAUR, CSIC, MCIN and AEI 10.13039/501100011033 under projects PID2023-151307NB-I00, PIE 20215AT016, and CEX2020-001058-M. MG is supported by the European Union's Horizon 2020 research and innovation programme under ERC Grant Agreement No. 101002652 (BayeSN; PI K. Mandel). N.R. is supported by a Northwestern University Presidential Fellowship Award. Zwicky Transient Facility access for N.R. was supported by Northwestern University and the Center for Interdisciplinary Exploration and Research in Astrophysics (CIERA). A.G. acknowledges financial support from the research project grant "Understanding the Dynamic Universe" funded by the Knut and Alice Wallenberg under Dnr KAW 2018.0067, Vetenskapsrådet, the Swedish Research Council through grants project Dnr 2020-03444.

References

Abdalla, E., Abellán, G. F., Aboubrahim, A., et al. 2022, Journal of High Energy Astrophysics, 34, 49

Abdul Karim, M., Aguilar, J., Ahlen, S., et al. 2025, Phys. Rev. D, 112, 083515

Abdul Karim, M. et al. 2025, Phys. Rev. D, 112, 083515

Amenouche, M., Rosnet, P., Smith, M., et al. 2025, A&A, 694, A3

Bellm, E. C., Kulkarni, S. R., Graham, M. J., et al. 2019, PASP, 131, 018002

Betoule, M., Kessler, R., Guy, J., et al. 2014, A&A, 568, A22

Blagorodnova, N., Neill, J. D., Walters, R., et al. 2018, PASP, 130, 035003

Bolejko, K., Nazer, M. A., & Wilshire, D. L. 2016, JCAP, 06, 035

Boubel, P., Colless, M., Said, K., & Staveley-Smith, L. 2025, J. Cosmology Astropart. Phys., 2025, 066

Carreres, B., Bautista, J. E., Feinstein, F., et al. 2023, A&A, 674, A197

Carreres, B., Rosselli, D., Bautista, J. E., et al. 2025, A&A, 694, A8

Célerier, M.-N. 2024, Phys. Rev. D, 110, 123526

Chen, G. C.-F., Fassnacht, C. D., Suyu, S. H., et al. 2019, MNRAS, 490, 1743

Cowell, J. A., Dhawan, S., & Macpherson, H. J. 2023, MNRAS, 526, 1482

Dekany, R., Smith, R. M., Riddle, R., et al. 2020, PASP, 132, 038001

Di Valentino, E., Mena, O., Pan, S., et al. 2021, Classical and Quantum Gravity, 38, 153001

Freedman, W. L., Madore, B. F., Hoyt, T. J., et al. 2025, ApJ, 985, 203

Fremling, C., Miller, A. A., Sharma, Y., et al. 2020, ApJ, 895, 32

Ginolini, M., Rigault, M., Copin, Y., et al. 2025a, A&A, 694, A4

Ginolini, M., Rigault, M., Smith, M., et al. 2025b, A&A, 695, A140

Graham, M. J., Kulkarni, S. R., Bellm, E. C., et al. 2019, PASP, 131, 078001

Guy, J., Astier, P., Baumont, S., et al. 2007, A&A, 466, 11

Guy, J., Sullivan, M., Conley, A., et al. 2010, A&A, 523, A7

Ishiyama, T. et al. 2021, Mon. Not. Roy. Astron. Soc., 506, 4210

Kalbouneh, B., Marinoni, C., Maartens, R., et al. 2025, arXiv e-prints, arXiv:2510.02510

Kim, Y.-L., Rigault, M., Neill, J. D., et al. 2022, PASP, 134, 024505

Kowalski, M., Rubin, D., Aldering, G., et al. 2008, ApJ, 686, 749

Kumar Aluri, P., Cea, P., Chingangbam, P., et al. 2023, Classical and Quantum Gravity, 40, 094001

Lacroix, L., Regnault, N., de Jaeger, T., et al. 2025, arXiv e-prints, arXiv:2509.04073

Masci, F. J., Laher, R. R., Rusholme, B., et al. 2019, PASP, 131, 018003

Mather, J. C., Cheng, E. S., Eplee, Jr., R. E., et al. 1990, ApJ, 354, L37

Migkas, K., Pacaud, F., Schellenberger, G., et al. 2021, A&A, 649, A151

Nusser, A. & Davis, M. 2011, ApJ, 736, 93

Peebles, P. J. E. 2025, Philosophical Transactions of the Royal Society of London Series A, 383, 20240021

Perley, D. A., Fremling, C., Sollerman, J., et al. 2020, ApJ, 904, 35

Phillips, M. M. 1993, ApJ, 413, L105

Planck Collaboration, Aghanim, N., Akrami, Y., et al. 2020, A&A, 641, A6

Riess, A. G., Yuan, W., Macri, L. M., et al. 2022, ApJ, 934, L7

Rigault, M., Aldering, G., Kowalski, M., et al. 2015, ApJ, 802, 20

Rigault, M., Neill, J. D., Blagorodnova, N., et al. 2019, A&A, 627, A115

Rigault, M., Smith, M., Goobar, A., et al. 2025a, A&A, 694, A1

Rigault, M., Smith, M., Regnault, N., et al. 2025b, A&A, 694, A2

Scolnic, D., Brout, D., Carr, A., et al. 2022a, ApJ, 938, 113

Scolnic, D., Brout, D., Carr, A., et al. 2022b, ApJ, 938, 113

Scolnic, D. & Kessler, R. 2016, ApJ, 822, L35

Stiskalek, R., Desmond, H., & Lavaux, G. 2025, arXiv e-prints, arXiv:2509.14997

The LSST Dark Energy Science Collaboration, Mandelbaum, R., Eifler, T., et al. 2018, arXiv e-prints, arXiv:1809.01669

Tony, J. L., Denneau, L., Heinze, A. N., et al. 2018, PASP, 130, 064505

Tripp, R. 1998, A&A, 331, 815

Tully, R. B., Kourkchi, E., Courtois, H. M., et al. 2023, ApJ, 944, 94

Verma, A., Patel, S. K., Aluri, P. K., Panda, S., & Mota, D. F. 2024, J. Cosmology Astropart. Phys., 2024, 071

¹ Université Clermont Auvergne, CNRS/IN2P3, LPCA, F-63000 Clermont-Ferrand, France

² Univ Lyon, Univ Claude Bernard Lyon 1, CNRS, IP2I Lyon/IN2P3, UMR 5822, F-69622 Villeurbanne, France

³ Institute of Astronomy and Kavli Institute for Cosmology, Madingley Road, Cambridge CB3 0HA, UK

⁴ Aix Marseille Université, CNRS/IN2P3, CPPM, Marseille, France

⁵ Centre Spatial de Liège, Université de Liège, Avenue du Pré-Ailly, 4031 Angleur, Belgium

⁶ School of Physics, Trinity College Dublin, College Green, Dublin 2, Ireland

⁷ Department of Physics, Duke University Durham, NC 27708, USA

⁸ Division of Physics, Mathematics and Astronomy, California Institute of Technology, 1200 E. California Blvd, Pasadena, CA 91125, USA

⁹ Department of Physics, Lancaster University, Lancaster, LA1 4YB, UK

¹⁰ Institute of Space Sciences (ICE-CSIC), Campus UAB, Carrer de Can Magrans, s/n, E-08193 Barcelona, Spain.

¹¹ Institut d'Estudis Espacials de Catalunya (IEEC), 08860 Castelldefels (Barcelona), Spain

¹² Division of Physics, Mathematics, and Astronomy, California Institute of Technology, Pasadena, CA 91125, USA

¹³ IPAC, California Institute of Technology, 1200 E. California Blvd, Pasadena, CA 91125, USA

¹⁴ The Oskar Klein Centre, Department of Astronomy, AlbaNova, SE-106 91 Stockholm, Sweden

¹⁵ Department of Astronomy & Center for Galaxy Evolution Research, Yonsei University, Seoul 03722, Republic of Korea

¹⁶ School of Physics, Trinity College Dublin, The University of Dublin, Dublin 2, Ireland

¹⁷ Instituto de Ciencias Exactas y Naturales (ICEN), Universidad Arturo Prat, Chile

¹⁸ School of Physics and Astronomy, University of Southampton, Southampton SO17 1BJ, UK

¹⁹ Sorbonne Université, Université Paris Cité, CNRS, Laboratoire de Physique Nucléaire et de Hautes Energies, 4 Place Jussieu, 75252 Paris, France

²⁰ Department of Physics and Astronomy, Northwestern University, 2145 Sheridan Road, Evanston, IL 60208, USA

²¹ Center for Interdisciplinary Exploration and Research in Astrophysics (CIERA), 1800 Sherman Ave., Evanston, IL 60201, USA

²² NSF-Simons AI Institute for the Sky (SkAI), 172 E. Chestnut St., Chicago, IL 60611, USA

²³ Caltech Optical Observatories, California Institute of Technology, Pasadena, CA 91125, USA

²⁴ Institut für Physik, Humboldt-Universität zu Berlin, Newtonstr. 15, 12489 Berlin, Germany

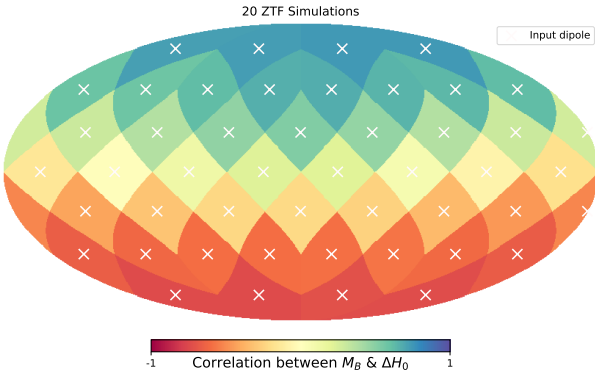


Fig. A.1. Skymap of the correlation between the parameter M_B , and the dipole amplitude, each white cross corresponds to a different location of dipole introduced in the data with the m_B method, for the 20 simulations with an initial amplitude of dipole of $3 \text{ km s}^{-1} \text{ Mpc}^{-1}$. Each patch is colored depending of the median of the correlation between the two parameters for the 20 simulations.

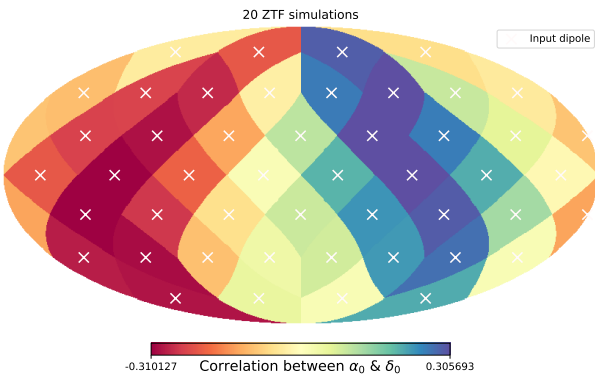


Fig. A.2. Skymap of the correlation between the parameter the α_0 and δ_0 of the dipole, each white cross correspond to a different location of dipole introduced in the data with the m_B method, for the 20 simulations with an initial amplitude of dipole of $3 \text{ km s}^{-1} \text{ Mpc}^{-1}$. Each patch is colored depending of the median correlation between the two parameters for the 20 simulations.

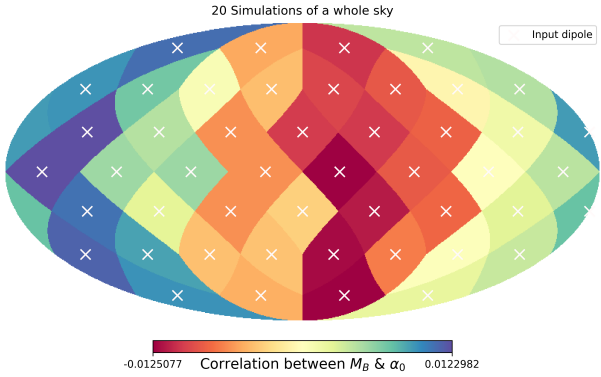


Fig. A.3. Skymap of the correlation between the parameter the α_0 and M_B for each dipole direction, each white cross correspond to a different location of dipole introduce in the data with the m_B method, for the 20 simulations of the all sky with an initial amplitude of dipole of $3 \text{ km s}^{-1} \text{ Mpc}^{-1}$. Each patch are colored in function of the median of the correlation between the two parameters for the 20 simulations.

retrieving the dipole right ascension α_0 . In comparison, for the declination δ_0 , we are biased of $\approx 1.3^\circ$ for the sky coverage with the ZTF footprint and the ZTF observing log, compare to the four other case where the bias is lower than 1° . We can suppose that the difficulty in recovering the signal for the amplitude near the equatorial pole comes from the cadence of the observation and not from the lack of observations below -30° . As presented in Appendix A, we believed that the oscillations were caused by the MW, but as seen in Fig.B.1 they are present for all the different sky coverage even an isotropic SN Ia distribution. However, these oscillations are included in the error as we can see for 40 simulations of the full sky in Fig. B.2. As we focus on the origin of oscillations we did 40 simulations with skysurvey, but we use the light curve parameters generated and we don't fit them. However, as mentioned in Sec. 5, these oscillations do not affect our analysis.

Appendix A: Correlation between fitted parameters

As explained in Sec. 3.2, we have to fit the standardization parameters at the same time as the dipole parameters due to the correlation between M_B and H_0 which introduced a correlation between M_B and the dipole amplitude as we can see in Fig.A.1. We have a strong correlation in all the sky for these two parameters. However, we also have a smaller one between the α_0 and δ_0 of the dipole, as shown in Fig.A.2. This correlation is larger near the Milky Way (MW) which also corresponds to the maximum and minimum of the oscillations discuss in Sec. 5. The mask on the MW makes it harder to constrain the dipole position. Fig. A.3 shows a clear correlation between the parameters M_B and α_0 in the area of the maxima and minima of the oscillations.

Appendix B: Results for α_0 and δ_0 for different sky coverage

To investigate in the origin of possible bias, we do the analyses in different sky coverage in Sec. 4.2, but we only present the result for the amplitude of the dipole. In this section, with the Fig. B.1, we present the result of α_0, δ_0 for the five different scenarios of sky coverage. In the different cases, we are unbiased in

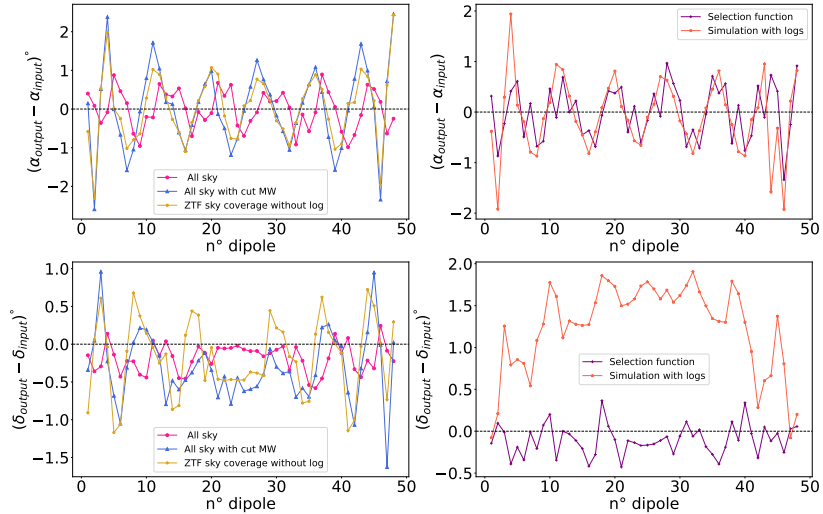


Fig. B.1. Comparison between three sky coverage. The results for a full sky, an uniform dispersion of SNe Ia, is represented in dark pink dot. The blue triangles correspond to simulations of the full sky but with a cut on MW. The pink stars represent simulations with a cut on MW and on declination but without logs. For all the simulation we didn't use the SALT parameters but the simulated light curve parameters.

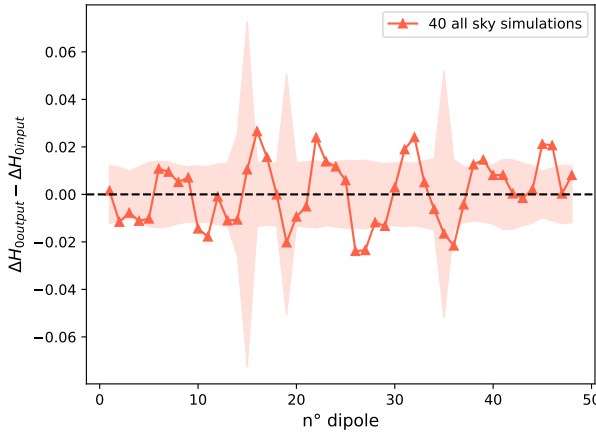


Fig. B.2. Difference between output and input of the amplitude of the dipole for 40 independent simulations of the full sky in function of the initial dipole introduced. With a orange band which is the error of the median (the standard deviation divided by the number of simulations).